

Title No. 121-S27

Behavior of Shear-Critical Concrete Deep Beams Monitored with Digital Image Correlation Equipment

by Dhanushka K. Palipana and Giorgio T. Proestos

This paper discusses the behavior of large-scale reinforced concrete deep beams that failed in shear and were monitored with full field-of-view, digital image correlation (DIC) equipment. Six shear-critical deep beams, measuring 4.88 x 1.11 m, were tested to failure. The specimens were point-loaded and simply supported, with three members examining the influence of asymmetrical loading conditions. The members were tested with various loading plate sizes and shear span-depth ratios. High-resolution displacement and strain field data obtained throughout loading are used to examine the member response. Principal compressive strain field diagrams of the deep beams at peak load are discussed. The paper presents crack patterns and crack kinematics, including crack widths and crack slips along critical shear cracks, determined from the DIC data throughout loading. The paper discusses crack dilatancy—that is, crack slips versus crack widths—along critical shear cracks, throughout loading, and at multiple locations. The results improve understanding of the detailed displacement field response of large shear-critical reinforced concrete deep beams, which can be used to improve kinematic and constitutive models, such as aggregate interlock models, for large-scale members.

Keywords: asymmetrical loading; deep beams; digital image correlation (DIC); disturbed regions; experiments; reinforced concrete; shear.

INTRODUCTION

Reinforced concrete deep beams such as transfer girders in high-rise buildings, corbels, and bent caps in bridges are used to transfer large loads (refer to Fig. 1). These “disturbed regions” have small shear span-depth ratios, typically less than 2.5, and the strain distributions through their depth are nonlinear. Therefore, beam theory becomes insufficient to predict response, and more refined methods are needed to describe the behavior.¹⁻³ In practice, these reinforced concrete structural elements can be subjected to symmetrical as well as asymmetrical loading. That is, some members may be point-loaded in the center of their spans; in other cases, the loading elements may be offset from the center of the spans, or lateral loads can give stress resultants from supported members acting away from the midspan of the deep beams (refer to Fig. 1).

Often, as a part of maintenance programs and evaluating the degradation of aging concrete infrastructure, these structural elements can require inspections or monitoring to ensure their suitability for continued use. Cracking is an important indicator of distress and the level of safety in concrete members. Often, visual inspections are carried out, and the crack widths are compared with the allowable limits in codes and guidelines.^{4,5} The recommended limits on crack widths are often not structure-specific and may only give general categorizations.

Additionally, some of the guidance documents do not distinguish between shear cracks and flexural cracks. This makes it difficult for engineers to interpret crack information. The literature has also explored various approaches for the assessment of structures from the perspective of damage indexes.⁶ In scenarios where more complex analyses are conducted, engineers can compare observed crack widths, crack slips, and crack shapes with predictions from nonlinear models and finite element tools. While these approaches can provide important information when conducting assessments, there are often issues reconciling the crack shapes observed with crack shapes in models, as well as reconciling observed crack widths and slips with model predictions. Thus, a better understanding of the detailed response of deep beams, including how the crack widths and slips vary along the critical cracks and throughout loading, particularly for large-scale members, is important.

Shear failures in concrete deep beams are brittle compared to flexural failure modes; therefore, when assessing such members, it is important to correctly interpret crack information that may be observed. Shear cracks in reinforced concrete deep beams develop at approximately two-thirds of their ultimate strength and often develop under service conditions. Thus, it is common to observe fully developed shear cracks in deep concrete beams during inspections.⁷ This often raises questions as to the safety of the members. To improve the methods by which concrete deep beams that exhibit shear cracking are assessed, methods that directly input the crack information, including the crack shape, width, and slip, are needed to determine structural safety. Additionally, as field inspection technologies and measurement techniques improve, interpreting detailed crack data, including the crack shape, widths, and slips, becomes more important.⁸ Some researchers report crack widths at a single location or the maximum crack width; however, the literature contains very limited, if any, data for large-scale shear-critical deep beam experiments that present the detailed kinematics of the cracks at multiple locations throughout loading.⁹⁻¹¹

To help improve assessment methods for shear-critical reinforced concrete deep beams and to better understand the behavior of cracks in deep members throughout loading, this paper presents a series of six large-scale, monotonically

ACI Structural Journal, V. 121, No. 2, March 2024.

MS No. S-2023-134.R1, doi: 10.14359/51740253, received September 19, 2023, and reviewed under Institute publication policies. Copyright © 2024, American Concrete Institute. All rights reserved, including the making of copies unless permission is obtained from the copyright proprietors. Pertinent discussion including author's closure, if any, will be published ten months from this journal's date if the discussion is received within four months of the paper's print publication.

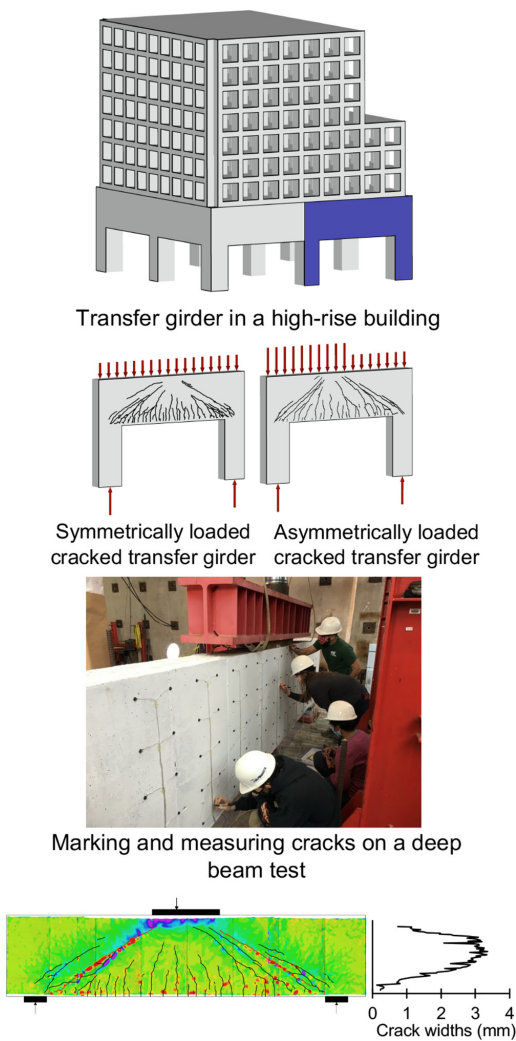


Fig. 1—Transfer girder in high-rise building; symmetrically and asymmetrically loaded cracked transfer girders; marking and measuring cracks on deep beam test; and compressive strain fields obtained using DIC, and crack pattern and widths obtained using DIC data.

loaded deep beams monitored using a full field-of-view three-dimensional (3-D) digital image correlation (DIC) system. Given the importance of testing large-scale members, as a result of the size effect in shear, the experimental program and measurements presented are important to improve the understanding of shear-critical deep beams and inform models appropriate for large-scale members.¹²⁻¹⁴ DIC techniques can be used to obtain high-resolution displacement field data over the entire specimen, throughout loading, in laboratory settings. DIC is a noncontact, optical data acquisition method that can be used to measure the two-dimensional (2-D) and 3-D displacement fields on the specimen surface subjected to loads (refer to Fig. 1). A speckle pattern is applied on the surface of the object, and cameras record the characteristics of the surface in image pixels. DIC analysis software tracks the subsets of pixels based on their unique gray value information using an image correlation algorithm. The quality of DIC data depends on the hardware configuration, test setup, quality of calibration, and user care. The image contrast, size and randomness of

the speckle pattern, and lighting conditions can also affect the quality of data obtained. DIC techniques provide more refined (higher-resolution) data than other displacement measurement techniques, such as infrared light-emitting diodes (LEDs), strain gauges, linear variable differential transformers (LVDTs), or other discrete displacement measurement approaches.^{15,16}

For the experiments presented in this paper, six high-resolution cameras (three sensor pairs) were used in tandem to capture the detailed displacement field of the entire surface of the large-scale deep beams. The paper first presents high-resolution displacement and strain field data obtained throughout loading and discusses member response in the context of the detailed measurements observed. The displacement and strain field data are then used to obtain crack patterns and crack kinematics for the critical shear cracks. The paper also discusses how the crack widths vary along the height of the specimens and the observed crack dilatancy throughout loading. The results of the data and experimental program can be used to inform codes and standards, such as ACI 318-19,¹⁷ AASHTO LRFD,¹⁸ CSA A23.3:19,¹⁹ ACI 224R-01,⁴ and the AASHTO Manual for Bridge Element Inspection.⁵ An analytical evaluation of the specimens can be found elsewhere.^{2,3,20}

RESEARCH SIGNIFICANCE

This paper presents a series of six large-scale shear-critical deep beam experiments monitored with high-resolution, full field-of-view, 3-D DIC equipment. The displacement fields and strain fields over the entire surface of the specimens were obtained throughout loading. Detailed displacement and strain field data are used to obtain crack patterns and crack kinematics up to failure. The results provide new insight into the complex behavior of shear-critical reinforced concrete deep beams.

EXPERIMENTAL PROGRAM

A series of six shear-critical deep beam tests, the CCR series, conducted at the Constructed Facilities Laboratory at North Carolina State University, Raleigh, NC, is examined in this paper. The beams measured 4877 mm long, 305 mm wide, 1105 mm deep, and had an effective depth of 909 mm. The longitudinal reinforcement consisted of No. 9 headed bars. Nine bars were used to reinforce the bottom of the beams, giving a longitudinal reinforcement ratio of 2.09%. Two bars were used to reinforce the top of the members in the compression region. Stirrups bent from No. 3 bars were placed at 330 mm along the span, giving a transverse reinforcement ratio of 0.141%. The specimen details for the CCR series of tests are shown in Fig. 2. The steel coupon test data, Young's modulus (E), yield stress (f_y), strain-hardening strain (ϵ_{sh}), ultimate strength (f_u), and strain at ultimate strength (ϵ_u) are shown in Fig. 3. These steel reinforcement ratios and steel material properties used are typical of a variety of structures, including bridge substructure components and transfer girders in buildings. The concrete cylinder strengths for the specimens (f'_c) are given in Table 1. It should be noted that a maximum coarse aggregate size (a_g) of 19 mm was used.

Table 1—Summary of CCR test specimen properties

Specimen	f'_c , MPa	a/d (north)	a/d (south)	l_{b1} , mm	Loading configuration
CCR1	34.5	2.25	2.25	610	Symmetrical loading
CCR2	35.8	2.00	2.00	610	Symmetrical loading
CCR3	39.5	1.80	1.80	610	Symmetrical loading
CCR4	37.8	1.80	2.25	914	Asymmetrical loading on symmetrical loading plate
CCR5	41.5	1.80	2.50	610	Symmetrical loading on asymmetrical loading plate
CCR6	39.3	2.11	2.39	914	Asymmetrical loading on symmetrical loading plate

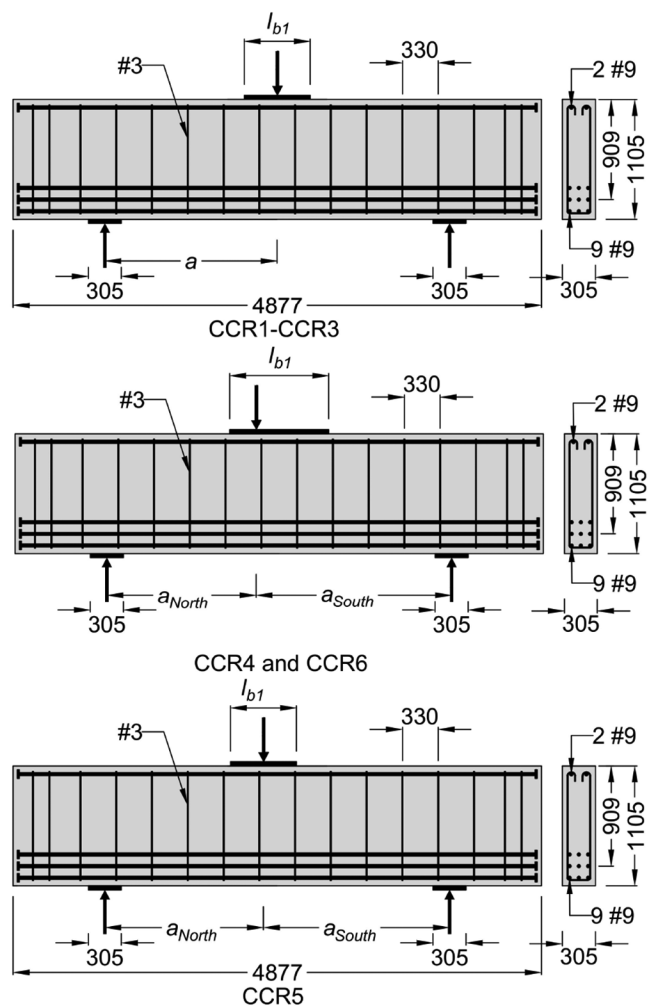


Fig. 2—Geometric and reinforcement details for CCR1 to CCR6. (Note: All dimensions are in mm.)

Deep beams often exhibit a critical shear crack that extends from the inner edge of the support plate to near the edge of the loading plate. This critical crack often has the largest crack widths on a given shear span and governs the response of the member. The critical loading zone is the highly compressed region under the loading plate that carries a substantial amount of shear.²¹ Varying the global critical crack angle and the size of the critical loading zone assists in investigating the behavior of deep beams by changing the key variables that influence related load-carrying mechanisms.^{9,22} Thus, the shear span-depth ratios (a/d) and the loading plate sizes (l_{b1}) were varied to observe the influence of the global critical crack angles and the size of the critical

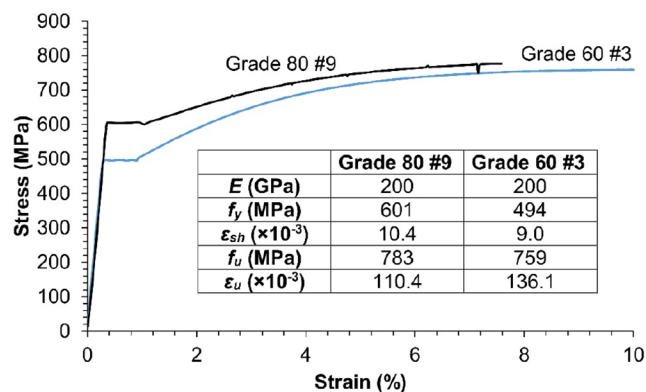
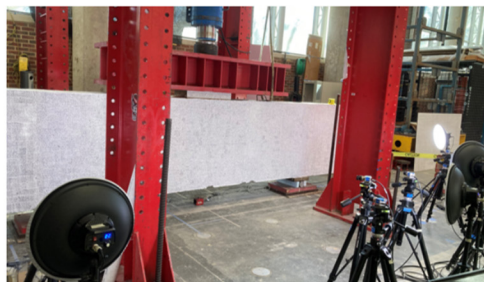


Fig. 3—Stress versus strain response of steel coupons and reinforcement properties.

loading zone on member response (refer to Table 1). These loading and supporting plate sizes are representative of a variety of structures and conditions, including conditions that may arise from columns supporting bridge substructure components and transfer girders supporting columns or walls in high-rise structures.

In addition to these variables, three loading configurations were explored. Specimens CCR1 to CCR3 were symmetrically loaded, where the load was centered on the loading plate and the loading plate was centered on the specimen. These specimens had the same l_{b1} (measuring 610 mm) and a/d ranging from 1.80 to 2.25. Specimens CCR4 to CCR6 were asymmetrically loaded. For CCR4 and CCR6, the load was applied 203 mm and 127 mm offset from the center of the symmetrically arranged loading plates, respectively. For CCR5, the loading plate was offset 318 mm from the center of the beam, and a load centered on the plate was applied. Specimens CCR4 to CCR6 were tested to examine the influence of asymmetrical conditions on the member response. Therefore, these loading arrangements represent symmetrical loading as well as asymmetrical loading conditions that can be the result of architectural requirements, geometrical constraints, or lateral loads that may act on structures.

To obtain high-resolution, full field-of-view deformation data, the entire surface of the west face of the beam was monitored with a full field-of-view 3-D DIC system. A resolution of approximately 2 pixels/mm was maintained using three stereo systems with two 12.3 megapixel cameras in each system (shown in Fig. 4 [top]). The data from the three systems was combined using a multi-view registration algorithm. A speckle pattern with speckles measuring approximately 2.5 mm in diameter was applied to the specimens.



Collecting deformation data using DIC on the west face



229 mm x 229 mm LED grid used on the east face

Fig. 4—DIC and LED instrumentation on test specimens.

This arrangement resulted in 3 to 5 pixels per speckle. The speckle pattern was applied so that the beam had approximately 50% black-white contrast. This setup resulted in virtual strain gauge lengths of approximately 19 mm; however, this varied somewhat between experiments to accommodate the different clear span lengths. The DIC setup provided the equivalent of approximately 0.5 to 2.0 million strain gauges on the specimen surface. More importantly, the 3-D displacement field was captured for the entire specimen surface throughout loading.

The east face of the beam was instrumented with a 229 x 229 mm grid of 95 infrared LED targets arranged in five rows and 19 columns (shown in Fig. 4 [bottom]). These targets were tracked using a 3-D position tracking camera to capture the deformation response. This data was used to verify and validate the DIC deformation field data obtained.

All six specimens were simply supported. The support plates measured 305 x 305 x 51 mm and rested on roller supports. The loading plate measured l_{b1} x 305 mm x 76 mm, where l_{b1} is given in Table 1. A soft fiberboard sheathing was used between the loading plate and the beam to ensure the load was evenly distributed on the top surface of the beam. A spreader beam was used to distribute the load from the actuator to the loading plate. A spherical bearing was used between the actuator head and the spreader beam to ensure that moments were not transmitted through the actuator.

The specimens were loaded monotonically to failure. Load stages were periodically conducted, and crack comparator gauges were used to manually mark and measure the cracks on the east face of the specimens. In addition to the DIC photos, during the experiments, high-resolution photos were taken locally on the specimens.

GLOBAL RESPONSE OF CCR SPECIMENS

Initial loading resulted in flexural cracks on the tension side of the beam under the loading plate. As the load increased, flexural cracks extended toward the compression region. Shear cracks formed in the clear span. Increased load resulted in stable shear cracks that widened until failure. All

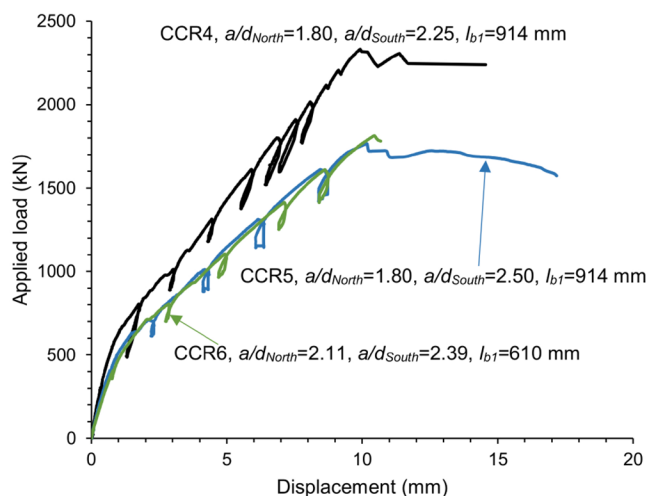
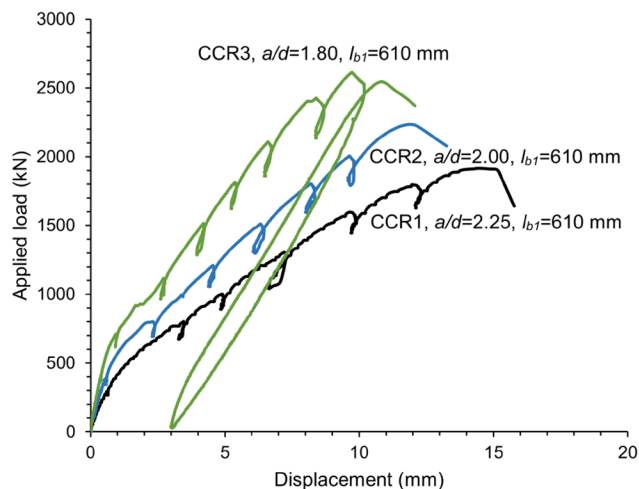


Fig. 5—Load versus beam displacement on flexural tension side at section under applied load for: (top) CCR1 to CCR3; and (bottom) CCR4 to CCR6.

specimens failed in shear. Specimens CCR1 to CCR3 and CCR6 exhibited an abrupt brittle failure, marked by shear crack widening and crushing near the critical loading zone. While CCR4 and CCR5 were also relatively brittle, they failed in a somewhat less abrupt manner. At the peak loads, the longitudinal bars of the specimen had not yielded. No splitting cracks were observed along the bottom of the beam.

The load versus displacement responses for all six specimens are shown in Fig. 5. The displacement on the flexural tension side of the beam at a section under the load was obtained from the DIC displacement field and accounts only for the relative displacement of the beam with respect to the supports. The top portion of Fig. 5 compares the response of CCR1 to CCR3, which are grouped as members with the same l_{b1} . The figure demonstrates that for specimens with the same l_{b1} , the strength of the specimen increases with decreasing a/d . The displacement at the peak load decreases with decreasing a/d . All specimens except CCR3 failed catastrophically and could not be reloaded. CCR3 was reloaded after reaching the peak load to determine the residual capacity. After unloading and reloading, the load does not exceed the first peak. This shows that the monotonic peak load of CCR3 was reached in the initial loading

Table 2—Summary of experimental results observed for CCR series

Specimen	Applied load at first flexural cracking, kN	Applied load at first shear cracking, kN	First cracking shear span	Peak load, kN	Peak shear force on failure span, kN	Displacement at peak load, mm	Failure span	Maximum crack width at peak load, mm	Maximum crack slip at peak load, mm
CCR1	238	768	North	1916	958	14.6	South	3.65	2.61
CCR2	226	752	North	2235	1118	11.9	North	4.70	4.33
CCR3	380	969	North	2614	1307	9.7	South	2.82	1.55
CCR4	293	973	South	2333	1296	9.9	North	2.29	1.97
CCR5	360	711	North	1765	739	10.2	South	2.33	1.14
CCR6	259	793	North	1816	964	10.4	North	2.82	1.87

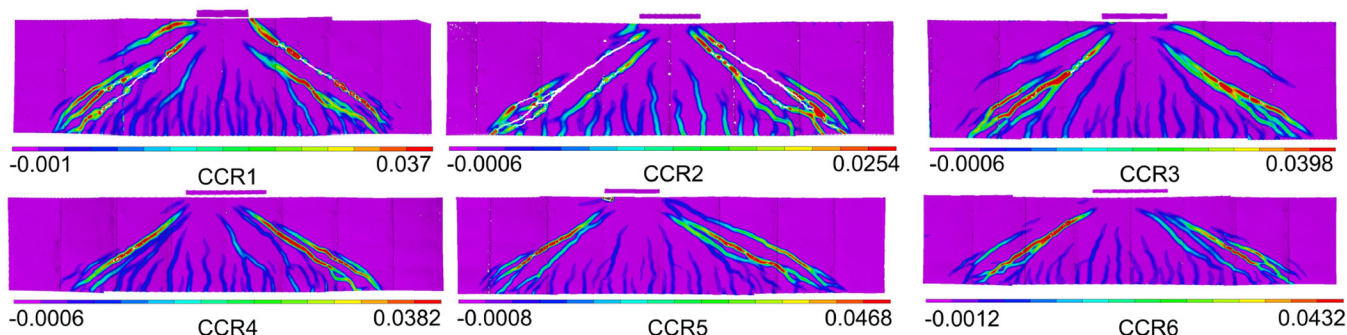


Fig. 6—Principal tensile strain fields (ϵ_1) at peak load for CCR1 to CCR6. (Note: Full-color PDF of this paper can be accessed at www.concrete.org.)

and is equal to the maximum applied load of 2614 kN. Figure 5 also examines the response of CCR4 to CCR6 and compares asymmetrically loaded members. Although CCR4 and CCR5 had the same a/d_{North} value and l_{b1} , the smaller a/d_{South} value for CCR4 resulted in a response with a higher peak load than CCR5. CCR5 and CCR6, which had different a/d and l_{b1} values, showed a similar response. This is likely from the combined effect of specimens with different a/d , l_{b1} , and specific crack geometries, resulting in different shear responses.^{9,22} That is, the combination of a/d , effective l_{b1} , specific crack geometry, crack widths, and crack slips contributed to the specific member response. The detailed response, including crack widths and slips, will be described in subsequent sections.

Table 2 provides a summary of the response of CCR1 to CCR6, including the values for first cracking, peak load, peak shear force on the failure span, displacement at the peak load, maximum observed crack width, and maximum observed crack slip. Typically, when two shear spans with different a/d and the same l_{b1} are considered, the shorter shear span has the higher strength.^{23,24} This was observed in CCR5, where the effective l_{b1} remained the same in both shear spans. The shear span of CCR5, which had a larger a/d , failed. However, for the CCR4 and CCR6 beams, the shorter shear span failed. For these members, although the a/d is smaller, the asymmetrical loading arrangement changes the effective l_{b1} and specific crack geometry, which results in a varied contribution of shear-transfer mechanisms.^{9,22} Therefore, although the shorter shear spans are typically expected to have higher strengths, when the loading is asymmetrical, the shorter shear span can be critical.

PRINCIPAL TENSILE AND COMPRESSIVE STRAIN FIELDS

Figure 6 shows a map of the principal tensile strain fields at the peak load for CCR1 to CCR6. The high-strain regions indicate the cracked regions. These tensile strain fields are used to develop crack diagrams, discussed in the next section. Figure 7 shows a map of the principal compressive strain fields at the peak load for CCR1 to CCR6. The strain fields show high compressive strains beneath and near the edges of the loading plates. The strains below the plate are not uniform and increase near the edges of the plate. This results from the compatibility of the rigid plate and the beam bending beneath it. These results are consistent with prior studies and are discussed elsewhere.^{25,26} For CCR6, the distribution under the plate is also influenced by the asymmetrical loading conditions. The diagrams also show the load arching from the loading plate to the support plates along compression struts. This behavior is typical of deep beams and demonstrates that the members are indeed disturbed regions. Additionally, the strain fields indicate that near the loading plates, the strains in the concrete exceed the strains at peak cylinder concrete stress. This is a result of the biaxial compression conditions that occur near the plates. For example, near the loading plate of CCR1, the largest principal compressive strain observed was -14.3×10^{-3} . It can also be observed that the strains along the compression struts that arch from the load are typically less than the strains at peak concrete cylinder stress. For instance, in specimen CCR6, the principal compressive strains observed along the struts were less than -2.1×10^{-3} .

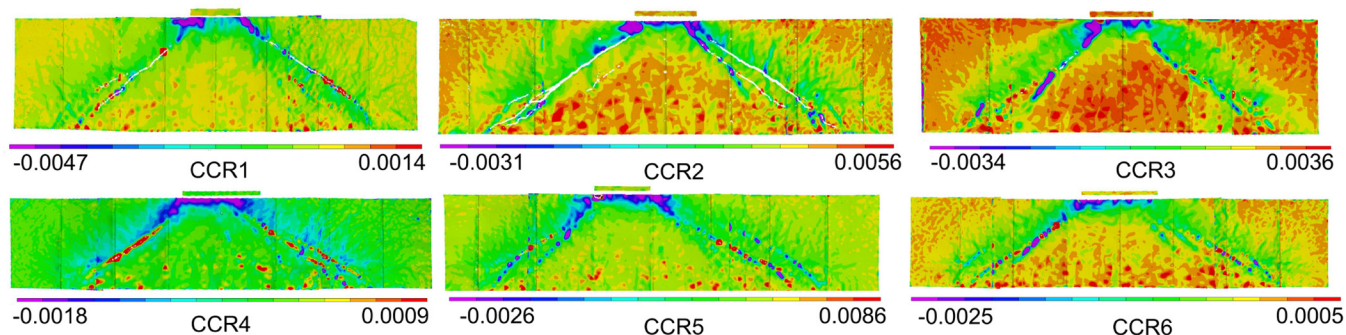


Fig. 7—Principal compressive strain fields (ϵ_c) at peak load for CCR1 to CCR6. (Note: Full-color PDF of this paper can be accessed at www.concrete.org.)

CRITICAL SHEAR CRACK KINEMATICS FROM DIC DATA

In this research, an open-source tool called the automated crack detection and measurement (ACDM) tool, developed by Gehri et al.,²⁷ was used to generate crack patterns from the DIC data. The principal tensile strains from the DIC data are input into the ACDM tool, which uses regions of high strains along with a mapping algorithm to detect and map the crack regions. Figure 8 (right) shows a summary of the crack patterns that were generated using the ACDM tool at the peak load for CCR1 to CCR6. These crack patterns are compared with the perspective-corrected photographs of crack patterns on the east face of the specimens in Fig. 8 (left), and they agree reasonably well. In some places, manual corrections were needed to correct minor discrepancies between the visually observed crack patterns and the outputs from the ACDM tool. The critical crack in reinforced concrete deep beams is typically the crack that extends from the inner edge of the support plate to near the edge of the loading plate. This crack typically has the largest crack width. The location and magnitude of crack widths were used to manually identify the critical cracks. The critical cracks were verified by comparing them with the visually observed crack patterns and crack widths on both faces of the specimen. In Fig. 8, the critical crack for CCR1 to CCR6 is shown in red for each shear span.

To obtain the local crack kinematics, namely the widths and slips, the critical crack was discretized into small crack segments. The critical crack was discretized using the intersection points of the crack on a grid equal to the maximum coarse aggregate size (19 mm). This crack discretization grid size was recommended by Trandafir et al.²² Then, for each crack segment (approximately 22 mm long), the crack kinematics were determined by considering the relative displacements of each of the two sides of the crack (refer to Fig. 9). A detailed discussion of how the crack kinematics were calculated for each crack segment is described in Langer²⁸ and Palipana et al.⁹ The reference points on either side of the crack were approximately 5 to 40 mm apart. Data points were selected so that they do not cross adjacent cracks or encroach on the boundary of cracks, where the DIC data can give spurious results. It should be noted that this discretization process and the determination of the crack kinematics is algorithmic and eliminates the need for manual interpretation of the crack data, thereby improving consistency.

First flexural and shear cracking

The crack patterns and the crack kinematics were used to determine the cracking response of the member, namely, identifying when the first flexural cracking and first shear cracking occurred. In the global response of the member, when the first flexural cracking occurs, the stiffness of the member gradually decreases from the elastic stiffness and tends toward the cracked elastic stiffness. This can be observed in the load versus displacement plots in Fig. 5. Table 2 summarizes the loads at which the first flexural cracking occurs for each specimen. A crack width of 0.05 mm was used as a minimum threshold to determine the first cracking because this can be visually verified during the experiment. CCR3 had the smallest a/d and the largest first flexural cracking load of 380 kN. CCR2, which had an a/d of 2.0, had the smallest first flexural cracking load of 226 kN.

A significant decrease in stiffness is observed when shear cracking occurs (refer to Fig. 5). Typically, shear cracks in deep beams are angled cracks that occur in the clear shear span. For consistent comparisons across the specimens, the load at which the first shear cracking occurs is taken as the load at which the critical shear crack reaches the midheight of the beam. A crack width of 0.05 mm was used as a minimum threshold to determine the first cracking because this can be visually verified during the experiment. The load at first shear cracking and the first shear span to exhibit shear cracking are given in Table 2. The principal tensile strain field diagrams for CCR1 to CCR6 at the first shear cracking load are shown in Fig. 10. The yellow ovals in Fig. 10 indicate the first critical shear crack identified.

The north shear span of CCR1 and the south shear span of CCR4 had an a/d of 2.25; the shear forces at which the first shear cracking occurs are 384 and 432 kN, respectively. CCR4 has a 13% higher shear cracking shear force than CCR1; this is likely attributed to the large effective l_{b1} . The north shear span of CCR3 and the north shear span of CCR5 had an a/d of 1.80. The shear forces at which the first shear cracking occurs are 485 and 413 kN, respectively. Thus, although CCR5 and CCR3 have the same a/d_{North} and l_{b1} value, CCR5 has a 15% lower shear cracking resistance than CCR3.

Crack widths and slips at peak load

For CCR1 to CCR6, the crack widths calculated from the displacement field for each crack segment are shown in Fig. 11 over the member height at the peak load. To verify

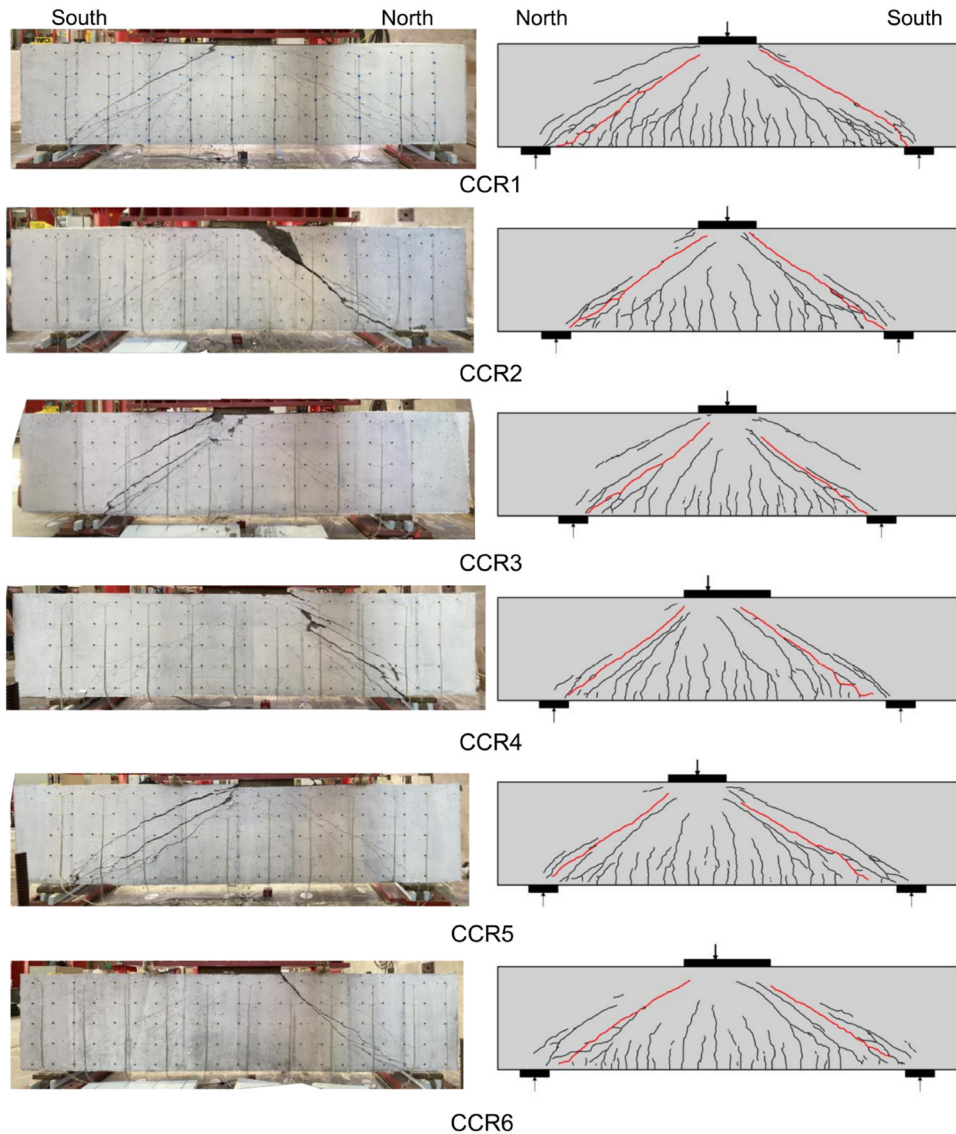


Fig. 8—(Left) Crack patterns on east face of specimens at failure; and (right) crack patterns obtained from DIC with critical crack highlighted in red for CCR1 to CCR6 at peak load. (Note: Full-color PDF of this paper can be accessed at www.concrete.org.)

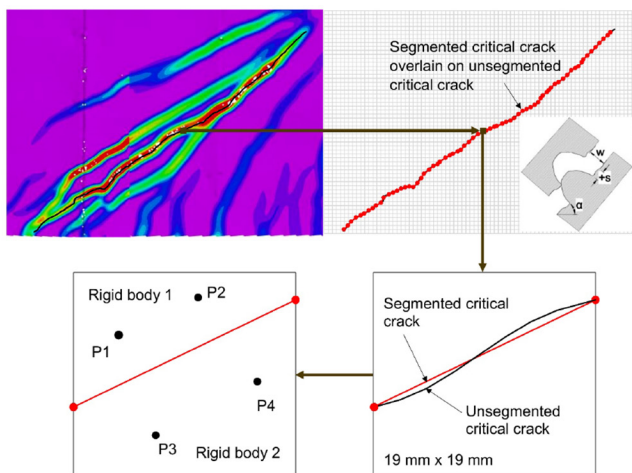


Fig. 9—Determining crack widths and slips on uniform grid (north shear span of CCR3).

and validate these results, Fig. 11 also shows the crack widths from the DIC data compared with the manually measured crack widths at the last load stage prior to failure. The differences between the manual measurements and crack widths from the displacement field data likely arise from subjective interpretations of crack widths and the local crack angles measured using crack comparators. Discrepancies may also arise from differences between the two surfaces measured, where nearby different secondary cracks may have influenced the crack widths of the critical crack.

Understanding the variation in the crack kinematics along the height of the beam is important to assist in conducting a detailed assessment of cracks. Specifically, being able to understand the variation in crack widths along member depth can help inform the relationship between maximum crack width and ultimate conditions, where the maximum crack width is expected to occur, and how the maximum crack width compares to cracks near the tension or compression region. As seen in Fig. 11, the crack widths are a maximum

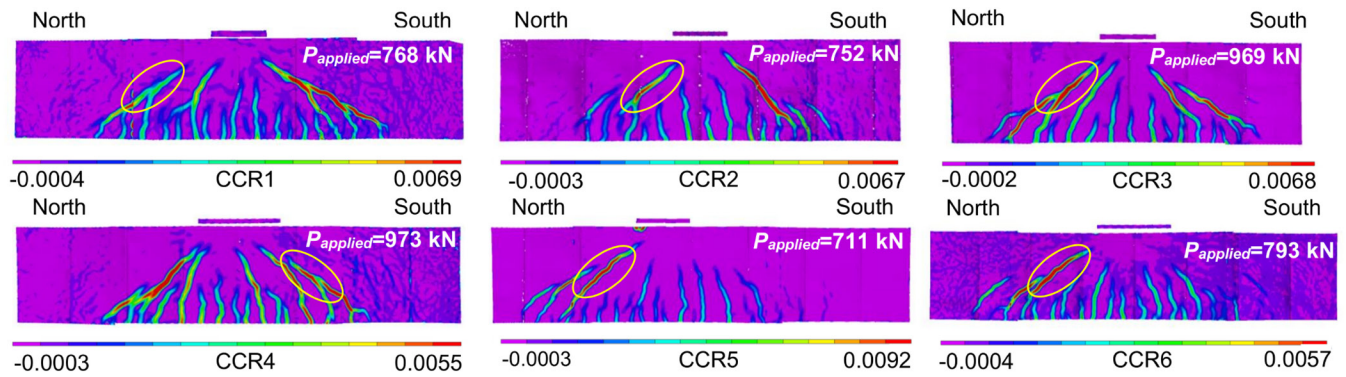


Fig. 10—Principal tensile strain fields (ϵ_1) at first shear cracking for CCR1 to CCR6. (Note: Full-color PDF of this paper can be accessed at www.concrete.org.)

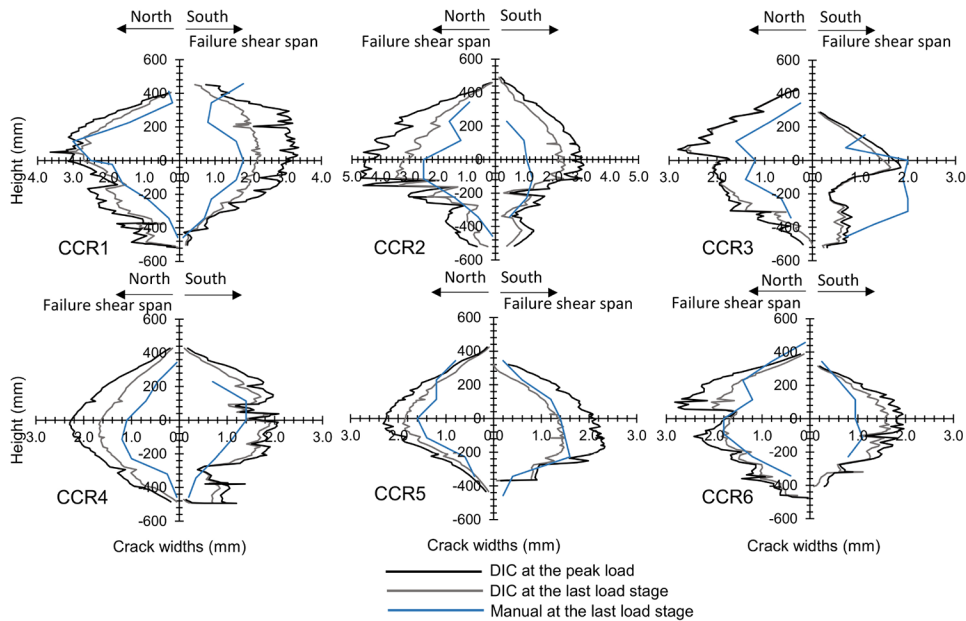


Fig. 11—Variation in crack widths with height along critical crack for CCR1 to CCR6 at last load stage and at peak load.

in the middle third of the section and decrease to a minimum near the top and bottom of the beam. This is consistent with the variation in crack widths along the height observed in previous studies.⁹ For the CCR series of tests, the maximum crack width is approximately 3.5 times the crack width at the height of the longitudinal reinforcement. The maximum crack widths observed for CCR1 to CCR6 at the peak load are given in Table 2.

The variation in crack slips is complex and depends on the local crack shape and the global kinematics of the beam projected onto the local crack. The maximum crack slips observed for CCR1 to CCR6 at the peak load are given in Table 2. The sign convention of crack slips is such that when the top face of the crack moves upwards, it is considered a positive slip (refer to Fig. 12). Here, w is the crack width, s is the crack slip, and α is the angle of the crack segment considered. Figure 12 shows the variation in crack slips of the south critical crack for specimen CCR2 at load stages 4 to 6 and at the peak load. As can be seen, the overall pattern of crack slips remains the same, but the magnitude of the slips increases with the load. The rapid variation in slips is not noise in the data and is consistent for increasing loads.

This rapid variation is due to the rapid variation in the local crack angle along the height of the member for the small crack segments used. To illustrate this, Fig. 12 also shows the crack angle of each crack segment for which the crack slip is plotted. The inset photo in Fig. 12 also shows that along a crack, the local angle can vary rapidly. Therefore, when the deformation field is projected onto these local axes, the values for slip can change rapidly from one crack segment to the next. The crack angle also has an influence on the variation in the crack widths, as seen in Fig. 11.

Figure 13 shows how the largest cracks vary with load for various crack segments. The solid lines correspond to the failure shear span for each specimen, and the dashed lines correspond to the non-failure shear span. The label for each curve indicates the specimen, the north or south shear span, and the a/d of the shear span. The crack widths are measured at the maximum crack width location of the critical crack on each shear span. For all the beams, this location is in the middle third of the height of the member. Once cracking occurs, the crack widths increase approximately linearly with the load. The rate at which the crack width increases varies for each shear span examined. For CCR1 and CCR3

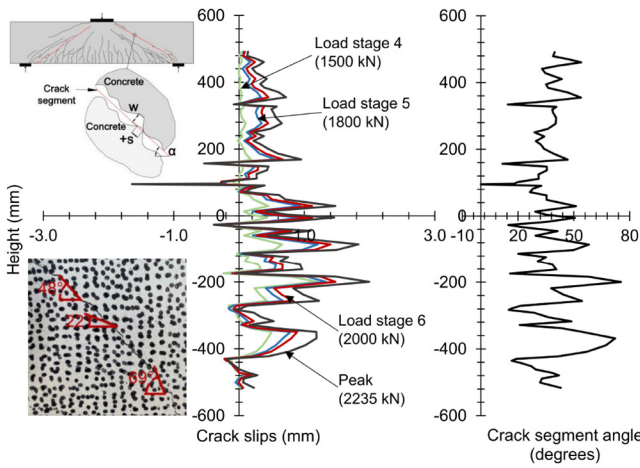


Fig. 12—Variation in crack slips and crack angle along height of CCR2 for south critical crack at load stages 4 to 6 and peak load.

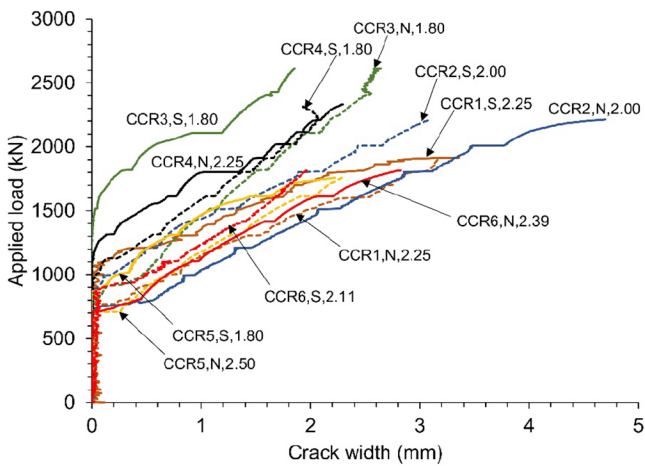


Fig. 13—Variation in crack widths with load for varying a/d . Label for each curve indicates specimen, north or south shear span, and a/d of shear span.

to CCR5, the non-failure shear span showed larger crack widths than the failure shear span at the maximum crack width location. For CCR2 and CCR6, the failure shear span showed larger crack widths than the non-failure shear span at the maximum crack width location. This observation demonstrates that determining the critical shear span solely based on the magnitude of the crack widths or using only limited measuring locations can yield insufficient structural assessments. Additionally, the maximum crack widths for the 12 shear spans vary from 1.85 to 4.70 mm at the peak load. Thus, interpreting the behavior of deep beams from crack information is complex, and the heuristic methods found in codes and guidance documents may not be sufficient to prioritize structural performance from crack information alone.

Figure 14 shows the variation in crack widths with crack slips throughout loading for nine crack segments in CCR1. The figure compares the response of crack segments at approximately the same location: near the midheight of the beam on the north shear span or the bottom of the critical crack in the south shear span (indicated by the green circles

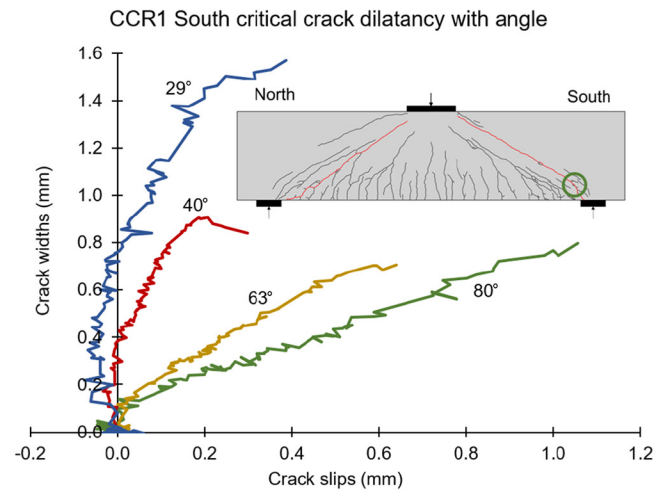
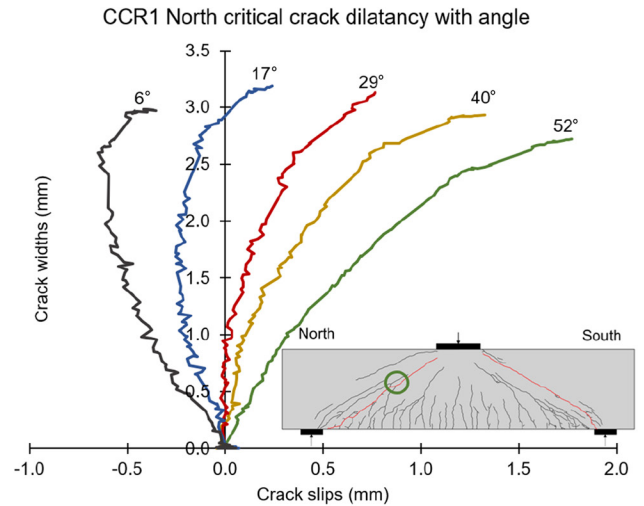


Fig. 14—Crack dilatancy throughout loading for CCR1 north critical crack and south critical crack.

in Fig. 14). By examining cracks near the same location in the member, the influence of the crack segment angle (α) on the variation in the crack width with crack slip throughout loading can be examined in isolation from the global kinematics of the beam. In Fig. 14, the number label for each curve indicates the angle of the crack segment with the horizontal axis (refer to α in Fig. 12). This variation in crack width with the crack slips, as the crack width grows, is called crack dilatancy and is important for formulating aggregate interlock models.²⁹⁻³¹

The crack dilatancy varies with the local crack angle, α , in a complex manner. First, for small angles, the crack slips increase in the negative direction with increasing crack widths. Then, the slips reach a maximum, and the cracks begin to slip in the opposite direction. Refer to the crack segments labeled 6 and 17 degrees for the north shear span of CCR1 and 29 degrees for the south shear span of CCR1 (Fig. 14). Second, for medium crack segment angles, the crack widths increase while the crack slips remain approximately zero. Then, the crack widths increase simultaneously with the crack slips. Refer to the crack segments labeled 29 degrees in the north shear span of CCR1 and 40 degrees in the south shear span of CCR1 (Fig. 14). For these crack

segments, the crack width versus crack slip behavior is similar to the crack kinematics proposed in the Guidotti aggregate interlock model.^{31,32} Specifically, the crack kinematics described in the Guidotti aggregate interlock model involve an initial pure crack opening, followed by a proportional increment of opening and sliding of the crack. The kinematic path described by Guidotti³¹ is consistent with observations shown for the cracks labeled 29 degrees in the north shear span of CCR1 and 40 degrees in the south shear span of CCR1 (Fig. 14). Third, as the crack segment angle increases, the crack slips increase positively with the crack widths. Refer to the lines labeled 40 and 52 degrees in the north shear span of CCR1 and the lines labeled 63 and 80 degrees in the south shear span of CCR1 in Fig. 14. This behavior of crack slips increasing positively with crack width is similar to the crack kinematic response in the aggregate interlock model proposed by Ulaga.^{32,33} Specifically, the crack kinematics described in the Ulaga aggregate interlock model involve a proportional increment of crack opening and sliding throughout loading. The kinematic path described by Ulaga³³ can be observed in the cracks labeled 40 and 52 degrees in the north shear span of CCR1 and the lines labeled 63 and 80 degrees in the south shear span of CCR1 (Fig. 14). For all the crack segments shown in Fig. 14, the slope of the curve decreases with increasing slips. These observations on crack dilatancy indicate that the local crack angle has a significant influence on the crack kinematic path and dilatancy. This suggests more advanced crack kinematic models accounting for these variations, including aggregate interlock models, could be developed for large-scale members to capture these differences in member response.

Figure 15 shows how the global kinematics of the member can influence the crack dilatancy for crack segments with the same local crack angle. In Fig. 15, the number label indicates the vertical distance from the top of the beam to the center of the crack segment; the locations of the segments are also shown on the inset diagram and circled in green. As can be seen from Fig. 15, when the crack segments are closer to the midheight of the specimen, where the crack widths are larger, they tend to show larger slopes in the crack dilatancy response. Away from the midheight of the specimens, either near the flexural compression or flexural tension region, the crack dilatancy slope decreases. Thus, in addition to observing differences in crack dilatancy for different local crack angles, the global kinematics of the members also influence the crack dilatancy of crack segments along the height of the specimens.

The nonlinear crack dilatancy response throughout loading has been explored by others, including Calvi et al.³⁴ and Ruggiero.³⁵ According to these authors, the nonlinear response of the crack dilatancy results from how the aggregate particles interact along the crack. Specifically, Calvi et al.³⁴ proposed that the crack evolves in a manner consistent with the shape of the steepest face of the aggregate particle. This shape of the steepest face of the aggregate particle is referred to as the local crack shape in this paper. Even for crack segments close to one another and with the same crack angle, it is possible that the local crack shape

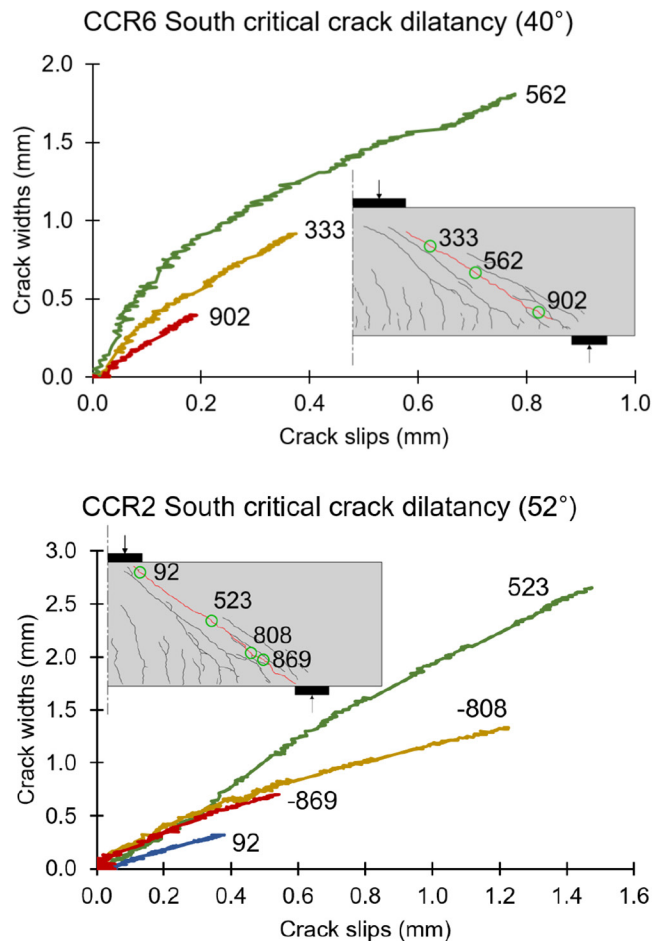


Fig. 15—Crack dilatancy for crack segments with same crack angle at different locations along critical crack for CCR2 and CCR6.

might differ. This can result in different crack dilatancies for cracks with the same approximate locations and the same crack angle. Calvi et al.³⁴ observed that initially, the increase in crack width and the crack slip are quite stiff due to compression at the contact points. Local crushing then occurs, changing the original crack surface. Calvi et al.³⁴ proposed that with further loading, as the local crack surface degrades, crack dilatancy softens. Therefore, degradation of the crack surface results in a nonlinear crack dilatancy response, where the crack width-crack slip ratio decreases as loading progresses. Calvi et al.³⁴ and Ruggiero³⁵ both tested panel elements subjected to uniform distributions of shear stress without the complexities of the moment. The results presented in Fig. 14 and 15 corroborate this explanation for crack dilatancy but for large-scale deep beam experiments. Therefore, other than the crack segment angle and the crack segment location along the crack, crack dilatancy likely depends on the shape of the aggregate at the contact points, local aggregate deformation due to crushing at the contact points, or a combination of both. The complex dilatancy responses observed indicate that more complex aggregate interlock models may be needed to capture the crack kinematic behavior of crack segments along the critical shear cracks in large-scale beam members.

CONCLUSIONS

This paper presents experimental results from a series of six large-scale shear-critical deep beam experiments monitored with full field-of-view digital image correlation (DIC) equipment throughout loading. The variables explored were shear span-depth ratio (a/d), loading plate size (l_{b1}), and loading configuration. All the specimens were monotonically loaded. With initial loading, flexural cracks occurred on the tension side of the beam under the loading plate. Further increase in the load resulted in shear cracks. Ultimately, all the specimens failed in shear. Typically, for beams with similar sections, as the shear spans get shorter, the strength of the member increases. However, it was observed that when a beam is asymmetrically loaded, the shorter shear span can be critical. The results also showed that as the a/d decreased, the ultimate strength of the specimens increased, and the displacement at the ultimate load decreased. The asymmetrically loaded specimens showed that the strength of the specimens and the failure span depend on the effective a/d and effective l_{b1} .

The paper presents high-resolution, full field-of-view displacement field data for all six deep beams, obtained from DIC measurements. Specifically, the paper presents the principal tensile and principal compressive strain fields obtained at the peak load. The tensile strain fields showed the flexural and shear cracked regions. The compressive strain fields showed highly compressed load-transfer paths and the compression struts that arch from the load to the supports. The compressive strains also showed the complex distribution of strains beneath the loading plates and the high strains located near the edge of the plates.

The DIC data and principal tensile strains were also used to generate crack patterns using the automated crack detection and measurement (ACDM) tool. The critical cracks were discretized, and the crack displacements, crack widths, and crack slips were calculated using the DIC displacement fields. The loads at which the first flexural cracking and shear cracking of the specimens occur were determined using the DIC data. The results showed that for shear spans with the same a/d , shear cracking forces can differ depending on the effective l_{b1} . The results also showed that even for shear spans with the same a/d and effective l_{b1} , shear cracking forces differed. The variation in crack widths along the height of the critical crack showed that the crack widths are largest near the middle of the section, away from the crack control provided by the longitudinal reinforcement or flexural compression region. It was shown that the crack slips vary rapidly along the height due to the rapid variation in the local crack angle along the critical crack. Results showed that the shear span with larger crack widths may not indicate the failure shear span.

The crack information obtained was then used to investigate crack dilatancy, the variation in crack widths with crack slips throughout loading. This paper presents, for the first time, crack dilatancy data for large-scale shear-critical deep beams. It was observed that the crack dilatancy varied depending on the crack angle and location of the crack segment in the member. For small crack angles, the crack slips increase in the negative direction with increasing

crack widths. They then reach a maximum crack slip, and then the crack slips increase in the positive direction. As the crack angle increases, the initial crack slips are close to zero, followed by an increase in crack slips positively with the crack widths. As the crack angles further increase, the crack slips and widths increase proportionally with loading. The crack segments closer to the midheight of the specimen, where the crack widths are larger, tend to show larger slopes in the crack dilatancy response. The crack dilatancy observations were consistent with previous research on panel tests subjected to pure shear and biaxial stresses. Specifically, the slope of the crack dilatancy curve changes continuously throughout loading, likely because of the degradation of the crack surfaces as the crack deforms.

The results in this paper show that the crack behavior of large-scale reinforced concrete deep beams is complex. Simply comparing crack widths with limits in codes and guidance documents or comparing limited measurement data to models can lead to inaccurate structural assessments. Therefore, a thorough understanding of crack kinematics is required when assessing large-scale structures based on cracks. While these complexities may not need to be considered in every analysis, understanding them may be needed to fully understand the shear behavior of deep concrete beams.

AUTHOR BIOS

ACI member **Dhanushka K. Palipana** is a Postdoctoral Researcher at the University of Kansas, Lawrence, KS. She is a member of Joint ACI-ASCE Subcommittees 445-E, Shear & Torsion-SOA Torsion, and 445-F, Interface Shear. She received her BSc Eng from the University of Peradeniya, Peradeniya, Sri Lanka, in 2017, and her PhD from North Carolina State University, Raleigh, NC, in 2023.

ACI member **Giorgio T. Proestos** is an Assistant Professor at North Carolina State University. He received his BSc in Engineering Science, MSc, and PhD from the University of Toronto, Toronto, ON, Canada, in 2012, 2014, and 2018, respectively. He is Secretary of Joint ACI-ASCE Committee 445, Shear and Torsion, and a member of Joint ACI-ASCE Subcommittee 445-E, Shear & Torsion-Torsion. He received the ACI Design Award in 2017 and the ACI Chester Paul Siess Award in 2018.

ACKNOWLEDGMENTS

The authors would like to thank Headed Reinforcement Corp. for their donation of headed reinforcing bars used in this experimental series.

REFERENCES

1. Mihaylov, B. I.; Bentz, E. C.; and Collins, M. P., "Behavior of Large Deep Beams Subjected to Monotonic and Reversed Cyclic Shear," *ACI Structural Journal*, V. 107, No. 6, Nov.-Dec. 2010, pp. 726-734.
2. Palipana, D. K., and Proestos, G. T., "Large-Scale Shear Critical Reinforced Concrete Deep Beam Experiments Monitored with Full Field of View Digital Image Correlation Equipment," *26th International Conference on Structural Mechanics in Reactor Technology (SMiRT-26)*, Division V, Berlin/Potsdam, Germany, July 2022, 10 pp.
3. Palipana, D. K., and Proestos, G. T., "Asymmetrical Loading of Reinforced Concrete Deep Beams Monitored with Full Field-of-View Digital Image Correlation," *Proceedings of the 14th fib PhD Symposium in Civil Engineering*, M. di Prisco, A. Meda, and G. L. Balázs, eds., Rome, Italy, Sept. 2022, pp. 105-112.
4. ACI Committee 224, "Control of Cracking in Concrete Structures (ACI 224R-01) (Reapproved 2008)," American Concrete Institute, Farmington Hills, MI, 2001, 46 pp.
5. AASHTO, "Manual for Bridge Element Inspection," second edition, American Association of State Highway and Transportation Officials, Washington, DC, 2019, 126 pp.
6. Woods, J. E.; Yang, Y.-S.; Chen, P.-C.; Lau, D. T.; and Erochko, J., "Automated Crack Detection and Damage Index Calculation for RC Structures Using Image Analysis and Fractal Dimension," *Journal of Structural*

Engineering, ASCE, V. 147, No. 4, Apr. 2021, p. 04021019. doi: 10.1061/(ASCE)ST.1943-541X.0002970

7. Zaborac, J.; Athanasiou, A.; Salamone, S.; Bayrak, O.; and Hrynyk, T. D., "Crack-Based Shear Strength Assessment of Reinforced Concrete Members Using a Fixed-Crack Continuum Modeling Approach," *Journal of Structural Engineering*, ASCE, V. 146, No. 4, Apr. 2020, p. 04020024. doi: 10.1061/(ASCE)ST.1943-541X.0002564

8. Spencer, B. F. Jr.; Hoskere, V.; and Narazaki, Y., "Advances in Computer Vision-Based Civil Infrastructure Inspection and Monitoring," *Engineering*, V. 5, No. 2, Apr. 2019, pp. 199-222. doi: 10.1016/j.eng.2018.11.030

9. Palipana, D. K.; Trandafir, A. N.; Mihaylov, B. I.; and Proestos, G. T., "Framework for Quantification of Shear-Transfer Mechanisms from Deep Beam Experiments," *ACI Structural Journal*, V. 119, No. 3, May 2022, pp. 53-65. doi: 10.14359/51734485

10. Peng, F.; Cai, Y.; Yi, W.; and Xue, W., "Shear Behavior of Two-Span Continuous Concrete Deep Beams Reinforced with GFRP Bars," *Engineering Structures*, V. 290, Sept. 2023, Article No. 116367. doi: 10.1016/j.engstruct.2023.116367

11. Silveira, M. V. G.; Paini, B.; Bitencourt, L. A. G. Jr.; and Das, S., "Design and Experimental Investigation of Deep Beams Based on the Generative Tie Method," *Engineering Structures*, V. 255, Mar. 2022, Article No. 113913. doi: 10.1016/j.engstruct.2022.113913

12. Bažant, Z. P., "Size Effect on Structural Strength: A Review," *Archive of Applied Mechanics*, V. 69, No. 9-10, Nov. 1999, pp. 703-725. doi: 10.1007/s0041900050252

13. Collins, M. P.; Quach, P. T.; and Bentz, E. C., "Shear Behavior of Thick Slabs," *ACI Structural Journal*, V. 117, No. 4, July 2020, pp. 115-126. doi: 10.14359/51724666

14. Trandafir, A. N.; Proestos, G. T.; and Mihaylov, B. I., "Detailed Crack-Based Assessment of a 4-m Deep Beam Test Specimen," *Structural Concrete*, V. 24, No. 1, Feb. 2023, pp. 756-770. doi: 10.1002/suco.202200149

15. Ulzurrún, G. S. D., and Zanuy, C., "Time-Variation of Shear Forces Affecting the Impact Resistance of Reinforced Concrete Beams," *Hormigón y Acero*, 2022, unpublished. doi: 10.33586/hya.2022.3088

16. Siebert, T.; Becker, T.; Spilthof, K.; Neumann, I.; and Krupka, R., "High-Speed Digital Image Correlation: Error Estimations and Applications," *Optical Engineering*, V. 46, No. 5, May 2007, Article No. 051004. doi: 10.1117/1.2741217

17. ACI Committee 318, "Building Code Requirements for Structural Concrete (ACI 318-19) and Commentary (ACI 318R-19) (Reapproved 2022)," American Concrete Institute, Farmington Hills, MI, 2019, 624 pp.

18. AASHTO, "AASHTO LRFD Bridge Design Specifications and Commentary," ninth edition, American Association of State Highway and Transportation Officials, Washington, DC, 2020, 1912 pp.

19. CSA A23.3:19, "Design of Concrete Structures," CSA Group, Toronto, ON, Canada, 2019, 301 pp.

20. Palipana, D. K., "Assessment of Shear Transfer Mechanisms in Reinforced Concrete Deep Beams from Experiments with Full Field-of-View Displacement Field Data," PhD thesis, North Carolina State University, Raleigh, NC, 2023, 440 pp.

21. Mihaylov, B. I.; Bentz, E. C.; and Collins, M. P., "Two-Parameter Kinematic Theory for Shear Behavior of Deep Beams," *ACI Structural Journal*, V. 110, No. 3, May-June 2013, pp. 447-456.

22. Trandafir, A. N.; Palipana, D. K.; Proestos, G. T.; and Mihaylov, B. I., "Framework for Crack-Based Assessment of Existing Lightly Reinforced Concrete Deep Members," *ACI Structural Journal*, V. 119, No. 1, Jan. 2022, pp. 255-266. doi: 10.14359/51733143

23. Ma, C.; Xie, C.; Tuohuti, A.; and Duan, Y., "Analysis of Influencing Factors on Shear Behavior of the Reinforced Concrete Deep Beams," *Journal of Building Engineering*, V. 45, Jan. 2022, Article No. 103383. doi: 10.1016/j.jobbe.2021.103383

24. Smith, K. N., and Vantsiotis, A. S., "Shear Strength of Deep Beams," *ACI Journal Proceedings*, V. 79, No. 3, May-June 1982, pp. 201-213. doi: 10.14359/10899

25. Proestos, G. T.; Palipana, D. K.; and Mihaylov, B. I., "Evaluating the Shear Resistance of Deep Beams Loaded or Supported by Wide Elements," *Engineering Structures*, V. 226, Jan. 2021, Article No. 111368. doi: 10.1016/j.engstruct.2020.111368

26. Qambar, M., and Proestos, G. T., "Experimental Investigation of Reinforced Concrete Deep Beams with Wide Loading Elements," *ACI Structural Journal*, V. 119, No. 4, July 2022, pp. 239-250. doi: 10.14359/51734497

27. Gehri, N.; Mata-Falcón, J.; and Kaufmann, W., "Automated Crack Detection and Measurement Based on Digital Image Correlation," *Construction and Building Materials*, V. 256, Sept. 2020, Article No. 119383. doi: 10.1016/j.conbuildmat.2020.119383

28. Langer, M., "Evaluation of the Load-Bearing Mechanisms in Coupling Beams and Shear Walls based on DIC Measurements," MSc thesis, University of Liège, Liège, Belgium, 2019, 136 pp.

29. Calvi, P. M.; Bentz, E. C.; and Collins, M. P., "Model for Assessment of Cracked Reinforced Concrete Membrane Elements Subjected to Shear and Axial Loads," *ACI Structural Journal*, V. 115, No. 2, Mar. 2018, pp. 501-509. doi: 10.14359/51701093

30. Cavagnis, F.; Fernández Ruiz, M.; and Muttoni, A., "An Analysis of the Shear-Transfer Actions in Reinforced Concrete Members without Transverse Reinforcement Based on Refined Experimental Measurements," *Structural Concrete*, V. 19, No. 1, Feb. 2018, pp. 49-64. doi: 10.1002/suco.201700145

31. Guidotti, R., "Poinçonnement des Planchers-Dalles avec Colonnes Superposées Fortement Sollicitées," PhD thesis, Thesis No. 4812, École Polytechnique Fédérale de Lausanne, Lausanne, Switzerland, 2010, 446 pp. (in French)

32. Campana, S.; Fernández Ruiz, M.; Anastasi, A.; and Muttoni, A., "Analysis of Shear-Transfer Actions on One-Way RC Members Based on Measured Cracking Pattern and Failure Kinematics," *Magazine of Concrete Research*, V. 65, No. 6, Mar. 2013, pp. 386-404. doi: 10.1680/macr.12.00142

33. Ulaga, T., "Betonbauteile mit Stab- und Lamellenbewehrung: Verbund- und Zuggliedmodellierung," PhD thesis, Thesis No. 15062, Zurich, Switzerland, ETH Zürich, Zürich, Switzerland, 2003, 167 pp. (in German)

34. Calvi, P. M.; Bentz, E. C.; and Collins, M. P., "Pure Mechanics Crack Model for Shear Stress Transfer in Cracked Reinforced Concrete," *ACI Structural Journal*, V. 114, No. 2, Mar.-Apr. 2017, pp. 545-554. doi: 10.14359/51689460

35. Ruggiero, D. M. V., "The Behaviour of Reinforced Concrete Subjected to Reversed Cyclic Shear," PhD thesis, University of Toronto, Toronto, ON, Canada, 2015, 455 pp.